Open Access

Design and Optimization of an Optofluidic Ring Resonator Based on Liquid-Core Hybrid ARROWs

G. Testa
G. Persichetti
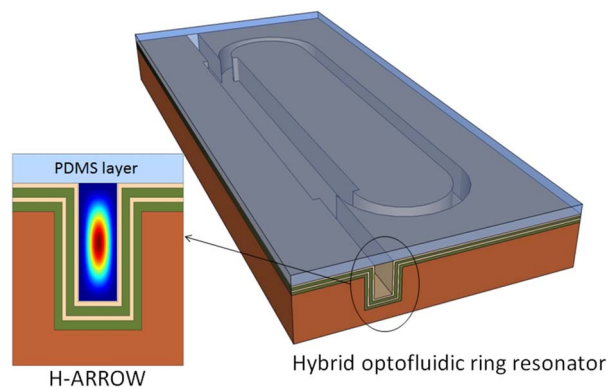**R. Bernini, Member, IEEE**

PDMS layer

H-ARROW

Hybrid optofluidic ring resonator

Design and Optimization of an Optofluidic Ring Resonator Based on Liquid-Core Hybrid ARROWs

G. Testa, G. Persichetti, and R. Bernini, *Member, IEEE*

Istituto per il Rilevamento Elettromagnetico dell'Ambiente (IREA), Consiglio Nazionale delle Ricerche (CNR), 80124 Naples, Italy

Abstract: In this paper, we present the design and analysis of an integrated optofluidic ring resonator based on liquid-core hybrid polymer-silicon antiresonant reflecting optical waveguide (h-ARROW). We perform a modal analysis of h-ARROW using the finite-difference method, in order to find the optimized optical configuration, which accomplishes single-mode operation and reduced attenuation losses. An accurate investigation of the bend sections is performed to preserve the single-mode behavior with reduced propagation losses. A hybrid liquid-core multimode interference (MMI) device is used as a coupling element in the ring layout, and three possible MMI configurations are simulated and compared. By properly designing and optimizing each optical element, we demonstrate, by simulations, the possibility to achieve a quality factor up to 4×10^4 with the extinction ratio of about 31 dB. Bulk and surface sensing performances of the device are also simulated and discussed.

Index Terms: Optical resonator, liquid core waveguides, ARROW, optofluidic, ring resonator.

1. Introduction

Ring resonator devices are of great interest in the field of optical sensing as it has been demonstrated by the impressive application results of the past few years [1]–[6]. Despite their compact size, ring resonators enable an enhanced limit of detection thanks to long interaction length resulting from resonances in the ring loop, which is assessed by the quality factor (Q-factor) of the ring cavity [7]. Integrated ring resonators with high optical performance can be fabricated by silicon technology [8], [9]. However, silicon based devices are not the best solution for microfluidic manufacturing, which is often hindered by expensive and complicated fabrication processes. Hybrid approaches that involve the combination of silicon-based optical and polymer-based microfluidic components have been successfully demonstrated and are becoming more and more widespread [6], [10]–[12]. Due to the huge potentiality of these devices in the field of sensing applications, a great deal of ongoing research is devoted to develop innovative approaches which integrate microfluidic functions into the microring itself in order to improve performances and make these devices more adaptable to lab-on-a-chip applications. In particular, a research area called optofluidic specifically addresses the way of how microfluidics interfaces with photonic elements at microscopic level [13], [14]. Highly promising optofluidic ring resonators (ORR)

based on whispering gallery modes (WGMs) have been recently demonstrated [15]. Very high Q-factor has been achieved with liquid core ORRs (LCORRs) based on micro-sized silica capillary [16], [17]. In these devices a thin wall microfluidic capillary acts as guiding element for the WGM and, at the same time, accomplishes the function of a microfluidic channel. Tubular rolled-up optofluidic ring resonators (RU-OFRRs) with good Q-factor have been fabricated and applied in array towards a fully integrated optofluidic sensor [11], [18]. Integrated ORRs based on slot waveguides and liquid core waveguides (LCWs) like ARROWs have been fabricated as well [2], [19].

LCWs are some of the most significant examples of optofluidic integration where the optical and microfluidic functionalities are closely and elegantly linked, as the core itself acts as microfluidic channel [20], [21]. ARROW waveguides in the hybrid version (h-ARROWs) have been recently proposed by our group as a possible solution to the problem of integration of microfluidic system with silicon optical device [22]. H-ARROW is constituted by the optofluidic channel of a conventional ARROW, sealed with a thin polydimethylsiloxane (PDMS) polymer layer. The PDMS layer has the optical function to confine the light in the core, but it could also perform microfluidic functions. The advantage of a h-ARROW as compared with conventional ARROW or other full-silicon LCWs, is that the upper PDMS layer can be used to integrate microfluidic system as a part of the waveguide itself, thus increasing the degree of compactness and integration. PDMS-based devices can be fabricated by using a simple and cost-effective fabrication process like soft lithography. Moreover, PDMS is optically transparent and allow us to illuminate and/or collect the light orthogonally to waveguide propagation axis. A first platform prototype based on h-ARROW, with microfluidic system integrated in upper PDMS multilayered structure, has been recently demonstrated from our group and tested for fluorescence measurements [23].

Here we report simulations, analysis and design of an integrated hybrid liquid core optofluidic ring resonator (h-LCORR) based on liquid core h-ARROWs. Simulation results show that optofluidic hybrid ring resonator with quality factor up to 4×10^4 could be achieved with a suitable design. These performances, together with the strong light-liquid interaction enabled by the optofluidic waveguides, permit to expect a limit of detection of $\triangle n_{min} \approx 3.7 \times 10^{-6}$. Moreover, the use of h-ARROW as basic waveguiding element simplifies further integration of microfluidic components, i.e., fluidic inlet and outlet and channels for delivering liquid sample, which could be cost-effectively and easily fabricated in PDMS layer. The proposed layout permits the h-LCORR to fully meet the requirement for an integrated optofluidic platform of incorporating microfluidic function.

2. Optofluidic Ring Resonator Design

2.1. Optofluidic Resonator Layout

Fig. 1 illustrates the schematic cross section of a hybrid ARROW the proposed device is based on. The waveguide hollow core defined in bottom silicon wafer is covered by antiresonant claddings and sealed by a PDMS layer.

A schematic layout of the ring resonator is shown in Fig. 2(a). Four 90°-curved h-ARROWs are used to form the resonator loop with a hybrid multi-mode interference (h-MMI) liquid core ARROW as coupling element between the ring and the bus waveguide. L_{MMI} and W_{MMI} are, respectively, the length and width of the MMI section, and d_c is the width of the waveguide core. A view drawing of the proposed h-ARROW optofluidic ring resonator is shown in Fig. 2(b). The device is constituted by two parts joined together. The bottom part is the optofluidic channel of ARROW, whereas the upper part is a single PDMS layer.

When ring resonators are used for sensing applications, sharp resonance and hence high-quality factor are desired in order to attain high sensitivity. It is well-known that the optical performances of a ring resonator strongly depend on the total ring round-trip losses which comprise both waveguide and coupling losses [7]. Therefore, we have focused our attention to design
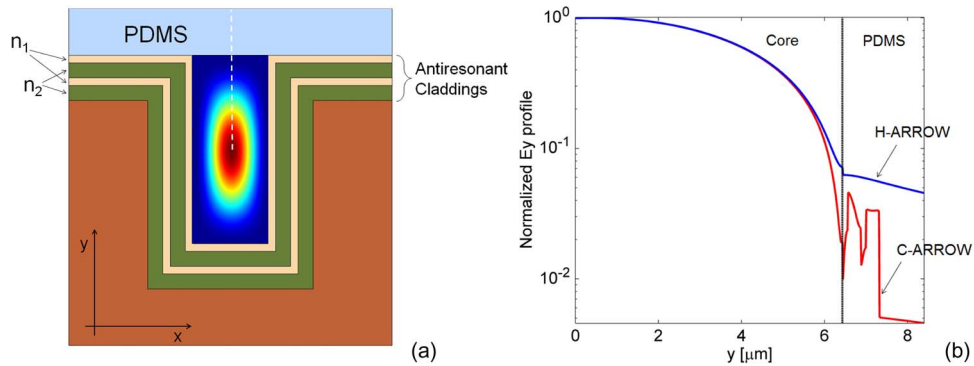
Fig. 1. (a) Schematic cross section of a h-ARROW waveguide with four antiresonant cladding layers with intensity profile of simulated fundamental mode. (b) Electric field profile along the y axes (white dashed line).
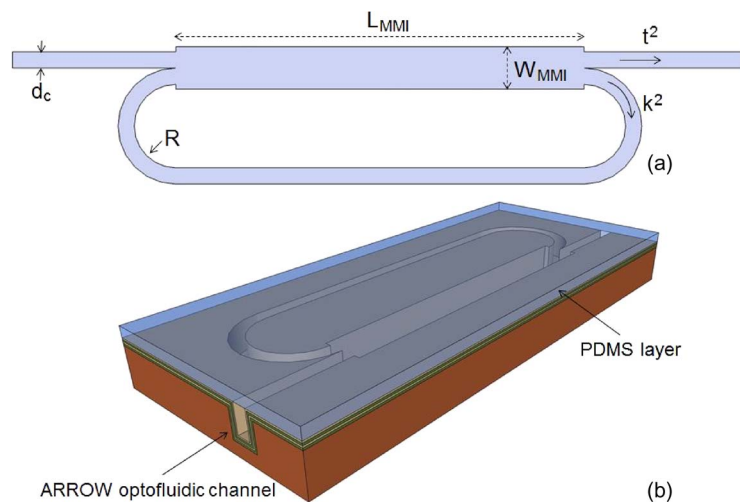

Fig. 2. (a) Schematic layout and (b) view drawing of the proposed hybrid ARROW optofluidic ring resonator.

and optimize each optical element of the proposed device in order to reduce the ring losses and obtain high-quality ring resonator.

2.2. Hybrid ARROW Waveguides Modal Analysis

ARROWs are very interesting optofluidic waveguides where the light is guided in a liquid core due to antiresonant cladding layers deposited on core sidewalls [20]. The antiresonance condition in the claddings corresponds to destructive interference phenomenon obtained by a proper choice of the layer thickness in order to fulfill the following condition [24]:

$$d_{1,2} = \frac{(2N+1)\lambda}{4n_{1,2}} \left[1 - \left(\frac{n_c}{n_{1,2}}\right)^2 + \left(\frac{\lambda}{2n_{1,2}d_c}\right)^2 \right]^{-\frac{1}{2}} \quad N = 0, 1, 2 \ldots \tag{1}$$

Conventional full silicon ARROW waveguides with only two cladding layers have been successfully applied for the realization of optical devices with good performances [19], [25]. However, the optical losses of the waveguide significantly decrease when more high- and low-index layers are added [26].

Compared to conventional ARROW, in the hybrid configuration the top multilayer is replaced with a single PDMS-layer [22]. The confinement property of such a hybrid structure can be explained by considering that ARROW losses strongly depend both on the core size and light polarization [27]. Since ARROW confinement is governed by Fresnel reflections, TM losses are much higher than the TE losses for the same core thickness. In particular, assuming an input polarization along the y axis, it can be considered as TE for the lateral confinement and TM for the transverse one. The substitution of top antiresonant cladding layers with a PDMS layer has an influence only on the TM losses, keeping unaffected the reflectivity for TE losses. In particular, for a h-ARROW with two anti-resonant layers and $n_c = 1.33$, the TM Fresnel reflection coefficient for the fundamental mode at the antiresonant cladding layers is $R_{TM} \approx 0.86$, while in the PDMS case it is $R_{TM}^H \approx 0.80$ [22]. This means that the substitution of antiresonant cladding layers with a PDMS layer has a small influence on the overall propagation losses. Moreover, to keep the TM losses low in the transverse direction, the height of the core is set wider, resulting in a rectangle cross section as shown in Fig. 1(a). As can be viewed in Fig. 1(a), the fundamental mode is well confined in the core of the proposed hybrid structure. In Fig. 1(b), the optical tail extending in the PDMS region is clearly visible. It explains the increased optical losses compared to the conventional configuration (C-ARROW). The optical performances of hybrid ARROWs have been experimentally studied in a previous work [22]. Propagation losses of 6.9 cm^{-1} were measured at the working wavelength of 635 nm, which rivals with the results obtained for a full-silicon ARROW. However, an extensive study of the hybrid configuration dedicated to the optimization of the optical performance has not yet been performed.

Numerical analysis of hybrid ARROW modes has been performed with a two dimensional mode solver [FIMMWAVE, Photon Design] by using the finite difference method (FDM). The waveguide has been designed to minimize the propagation loss for a water-filled core ($n_c = 1.330$) at a wavelength of $\lambda = 770$ nm. In the simulations, silicon nitride (refractive index $n_1 = 2.044$) and silicon dioxide ($n_2 = 1.441$) were considered as first and second cladding layer, respectively. The appropriate cladding layer thicknesses d_1 and d_2 have been calculated by using (1) with N = 0 for each fixed core width d_c. The refractive index of PDMS has been set to $n_P = 1.425$. Moreover, since the water absorption coefficient of about 0.02 cm^{-1} at $\lambda = 770$ nm is very low with respect to typical fundamental mode attenuation loss of ARROW waveguide, its contribution is neglected in the simulations. In order to find the optimal configuration with reduced propagation loss, three layouts with different number of bi-layer claddings are analyzed and discussed. In particular, hybrid structures with one (1h-ARROW), two (2h-ARROW), and three (3h-ARROW) high and low-index layers are simulated by varying the core width (d_c) and height (h).

The core size parameters considered in the simulations are $d_c = 2, 3, 4,$ and 5 μm and $h = 8, 10,$ and 12 μm. Fig. 3 illustrates the calculated fundamental mode attenuation losses α_0 for different core width (d_c) versus h. In Table 1 the fundamental mode losses α_0 versus d_c in the particular case of $h = 12$ μm are summarized. From these results we can observe that a strong loss reduction is obtained by moving from 1h-ARROW to 2h-ARROW configuration, but further addition of bi-layer (3h-ARROW) significantly affects the attenuation only for small d_c. This general rule applies also to conventional ARROW and it can be explained by considering that the light propagation in ARROW arises from Fresnel reflections at the core/cladding interfaces. Fresnel coefficients do not increase linearly with the number of cladding bi-layer; hence smaller improvements of the losses are obtained as more bi-layers are added. From Fig. 3, it can also be noticed that the losses strongly decrease by increasing the core height while they are less affected by the core width, especially when more bilayer are used. As mentioned before, this behavior is due to the strong polarization dependence of ARROW losses. In particular, for the fixed polarization, TM reflection coefficient of transverse cladding is always lower than TE reflection coefficient of lateral cladding, according to the Fresnel formula. For this reason, by increasing the ratio h/d_c, the total losses decrease very rapidly due to decreasing of the TM-component of the losses.

In ARROWs design it is also important to keep in mind the leaky nature of these waveguides. In fact, ARROW supports a quasi-single mode operation thanks to the loss discrimination of
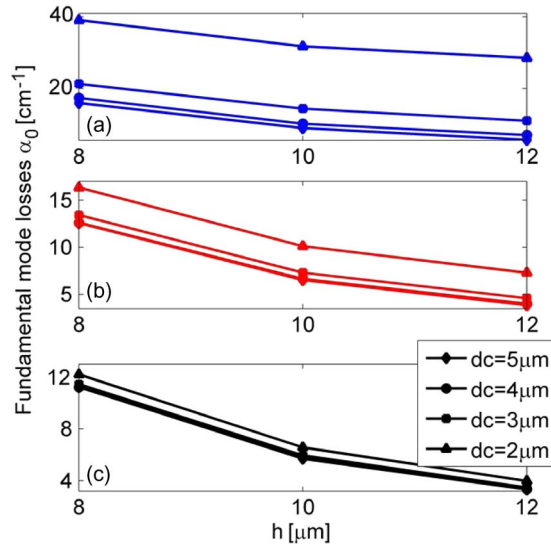
Fig. 3. Fundamental mode attenuation losses for different core width d_c versus h for the (a) 1h-ARROW, (b) 2h-ARROW, and (c) 3h-ARROW configurations.

TABLE 1

Fundamental mode attenuation losses $[\mathrm{cm}^{-1}]$ ($h = 12$ μm)

$d_c[\mu m]$	1h-ARROW	2h-ARROW	3h-ARROW
2	28.55	7.29	3.98
3	11.02	4.60	3.48
4	7.07	4.00	3.36
5	5.73	3.85	3.33

TABLE 2

Mode coupling coefficients ($h = 12$ μm)

$d_c[\mu m]$	c_0	c_{12}	c_{13}	c_{31}
2	0.32	5.79×10^{-3}	1.15×10^{-2}	1.64×10^{-2}
3	0.48	9.43×10^{-3}	1.78×10^{-2}	3.10×10^{-2}
4	0.62	12.60×10^{-3}	2.36×10^{-2}	3.59×10^{-2}
5	0.74	15.10×10^{-3}	2.87×10^{-2}	3.20×10^{-2}

higher order modes which experience lower reflection coefficient at the core/cladding interface. So, the optimization of core dimension of a single mode ARROW is the result of a compromise between low fundamental mode attenuation constant (α_0) and higher order modes filtering effect. For this reason, we analyze the attenuations and the coupling coefficients of the higher order modes, too. High order modes coupling coefficients and attenuations are designated as c_{mn} and α_{mn}, respectively, whereas c_0 and α_0 refer to the fundamental mode. To calculate the coupling coefficients we use a three dimensional eigenmode expansion method (EME). In the simulations, the field of a single mode fiber at $\lambda = 770$ nm with a full width at half maximum (FWHM) mode field diameter of 5 μm is considered as input field. We have calculated the power distribution among the relevant propagating modes by varying the core width d_c of a 2h-ARROW with core height $h = 12$ μm. Propagating modes which couple to less than 0.001% of the input power are neglected. The simulation results are summarized in Table 2.

TABLE 3

Mode attenuation losses $[\text{cm}^{-1}]$ $(h = 12 \ \mu\text{m})$

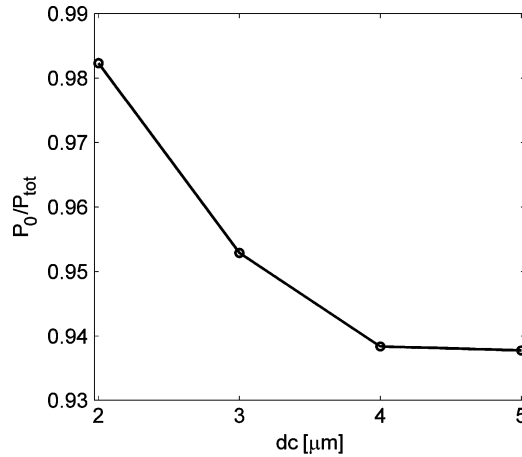| $d_c[\mu m]$	α_0	α_{12}	α_{13}	α_{31}
2	7.26	18.84	38.07	135.64
3	4.57	15.83	34.71	19.62
4	4.01	15.01	33.45	8.80
5	3.86	14.95	33.57	5.99

Fig. 4. Normalized power fraction coupled to the fundamental mode versus dc after a propagation distance of 500 μm.

It is clear that only a small part of the input power is coupled into higher order modes and that this coupling is always much lower than the one of the fundamental mode. However, in order to fully understand the contribution of the higher order modes to the total output power, the attenuation losses α_{mn} compared to that of the fundamental mode α_0 must be also taken into account. Attenuation losses versus d_c are summarized in Table 3 in the case of a 2h-ARROW with $h = 12 \ \mu$m.

As already mentioned, we observe that higher order modes attenuate faster than the fundamental one. This aspect, together with the fact that the amount of power coupled to these modes is quite low, results in a quasi-single mode operation of these waveguides after a propagation distance of few hundred microns. This behavior is shown in Fig. 4 where the power fraction coupled to the fundamental mode compared to the total power distributed among all the relevant propagating modes (P_0/P_{tot}) is plotted versus the core width after a propagation distance of 500 μm. As it can be expected, the degree of suppression of higher order modes improves as the core width decreases. In particular, for $d_c = 2 \ \mu$m more than 98% of the total power is coupled to the fundamental mode. Furthermore, P_0/P_{tot} reaches the minimum of 94% for $dc = 5 \ \mu$m, which is still high.

In conclusion of this paragraph, we can state that 2h-ARROW and 3h-ARROW configurations are both suitable for the realization of low loss liquid core waveguides. As it concerns to single mode operation, the power coupled to the higher order modes is always lower when compared with the fundamental mode. This aspect, together with the very high attenuation losses experienced by these modes, allows us to obtain quasi-single mode h-ARROW operation with core width up to 5 μm. About the fabrication tolerance, we estimated that a fabrication error of $\pm 0.1 \ \mu$m in waveguide width causes changes in the fundamental mode attenuation of about ∓ 0.6 cm^{-1} in the case of $d_c = 2 \ \mu$m.

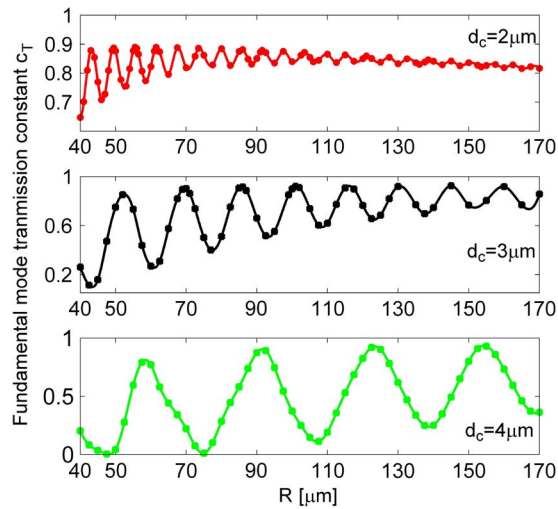In the following we limit our analysis to 2h-ARROW configuration with $h = 12 \ \mu$m.

Fig. 5. Fundamental mode power transmission coefficient as function of curvature radius for waveguide widths $d_c = 2, 3$, and 4 μm.

2.3. Bend h-ARROW Waveguide Design

The antiresonance confinement mechanism of ARROWs poses several problems in waveguide bend design. Hence, an optimized choice of the h-ARROW bend parameters is required to minimize bending losses.

The attenuation losses in the bend sections are calculated with a mono dimensional mode solver [FIMMWAVE, Photon Design] using the finite difference method. In the simulated layout, the bend section is a semi-circumference with curvature radius R connected with straight input and output ARROW waveguides. In the simulations, the appropriate fundamental mode of a straight ARROW waveguide was assumed as input field.

Due to bending, a significant part of the power carried by the fundamental mode of the input waveguide may be transferred to the higher order modes, especially at small curvature radius, thus deteriorating the ring performance. In order to estimate this effect, we have derived the amount of power transmitted from the fundamental input mode to the fundamental output mode of a straight waveguide after propagating along the bend section. The simulations are performed by varying R and d_c in order to find the optimized bend configuration, i.e., the one which preserves as much power as possible in the fundamental mode. In Fig. 5 we show the power transmission coefficients to the fundamental mode of the output straight waveguide (c_T) versus the curvature radius R for $d_c = 2, 3$, and 4 μm. As it can be noticed, the coefficient c_T varies in a damped oscillatory manner with the radius R. This phenomenon is the result of the multimodal interference between the modes excited in the bend section. In particular, wider ARROW waveguides exhibit higher order modes which propagate longer due to lower attenuation constant, thus enhancing the MMI effect. In all the explored cases, a curvature radius R^* exists, over which the oscillations are almost totally damped. The resulting bend length πR^* represents the propagating distance where the higher order modes are totally attenuated. As it can be noticed from Fig. 5, this effect takes place for high R. However, smaller radii with low bending losses can be achieved by selecting appropriated radii corresponding to the maxima of the curve for a given d_c. As an example, for $d_c = 2$ μm, c_T reaches 0.88 at around $R = 50$ μm. For $d_c = 3$ μm, the maximum of $c_T \approx 0.92$ corresponds to a curvature radius $R = 145$ μm (Fig. 5).

However, if the core width d_c is slightly off in the fabrication (e.g. ± 0.1 μm), a mismatch between R and d_c occurs, and thus bend transmission may not match a peak. We simulated the fabrication tolerance and found that, in the case of $d_c = 2$ μm, a deviation of 5% of d_c may cause a transmission reduction up to 17%, at around $R = 50$ μm.

TABLE 4

MMI Parameters $[\text{cm}^{-1}]$ ($h = 12$ μm)

$MMI\ Type$	$d_c[\mu m]$	$L_{MMI}[\mu m]$	$W_{MMI}[\mu m]$	t^2	k^2	α_c^2
A(50:50)	2	121	6	0.484	0.483	0.967
B(85:15)	2	322	8	0.775	0.126	0.901
C(72:28)	2	401	10	0.624	0.250	0.874
A(50:50)	3	215	8	0.490	0.481	0.979
B(85:15)	3	508	10	0.790	0.138	0.928
C(72:28)	3	581	12	0.696	0.260	0.956

Actually, the choice of the waveguide width d_c is the better compromise among several factors: the power transmission coefficient c_T, the fundamental mode propagation losses α_0, and the ratio c_0/c_{mn} between the coupling coefficient of the fundamental mode c_0 and the one of the higher order modes c_{mn}.

2.4. H-MMI Coupler Design

The coupling of light from the bus waveguide to the ring section is obtained with a liquid core 2h-ARROW-based multimode interference (MMI) coupler. Three MMI configurations at the working wavelength of $\lambda = 770$ nm and with a core refractive index $n_c = 1.330$ have been explored with different splitting ratios (t^2, k^2) between the two output ports [Fig. 2(a)]. In particular, splitting ratios of $50:50$ (type A MMI), $85:15$ (type B MMI), and $72:28$ (type C MMI), have been considered. The length of the MMI (L_{MMI}) depends on the square of the MMI width (W_{MMI}) [28], which in turns is related to the waveguide width d_c. Therefore, in order to have a compact device size we limit our analysis to bus waveguides of width $d_c = 2, 3$ μm.

Simulations have been performed in order to estimate the coupling factor $\alpha_c^2 = t^2 + k^2$, which in turn depends on the coupler length L_{MMI}. Table 4 lists the length of the MMI, the power transmission coefficients t^2 and k^2 and the power coupling factor α_c^2 in the particular case of a 2h-ARROW waveguide with input/output core width of $d_c = 2, 3$ μm. The transmittances of the MMI output waveguides are calculated using a two dimensional finite difference time domain method (2D FDTD) (OMNISIM, Photon Design). All the listed parameters are referred to the fundamental ARROW mode. Since higher order modes propagate with high attenuation losses, the image of the input field at the output due to the MMI effect could slightly degrade, especially for longer MMI sections. As a consequence, the power coupling factor α_c^2 decreases by increasing the propagation length (for a fixed d_c).

Concerning the fabrication tolerance, a deviation of ± 0.1 μm in both d_c and W_{MMI} causes the coupling factor to reduce up to about 15% and 4% in the case of MMI type A with $d_c = 2$ μm and $d_c = 3$ μm, respectively.

2.5. Ring Design

In the design of a ring resonator for sensing application, both high Q and deep resonance [i.e., large extinction ratio (ER)] are fundamental parameters.

For a resonator having power attenuation constant α_R^2 and coupling factor α_c^2, the transmitted power in the output waveguide is [7]

$$|T|^2 = \alpha_c^2 \frac{\alpha^2 - 2\alpha t \cos\theta + t^2}{1 - 2\alpha t \cos\theta + \alpha^2 t^2} \tag{2}$$

where $\alpha^2 = \alpha_c^2 \alpha_R^2$ is the single-pass power transmission which accounts for the total optical losses in the ring, including the propagation losses and the coupler losses, and θ is the total

TABLE 5

Estimated ring parameters

$MMI\ Type$	$d_c[\mu m]$	$R[\mu m]$	$L_R[\mu m]$	α_R^2	Q_{th}	$ER_{th}[dB]$
A(50:50)	2	50	556.16	0.733	5.485×10^3	8.779
B(85:15)	2	50	958.16	0.691	1.405×10^4	10.357
C(72:28)	2	50	1116.16	0.658	1.151×10^4	21.791
A(50:50)	3	145	1341.06	0.840	1.567×10^4	4.788
B(85:15)	3	145	1927.06	0.818	4.276×10^4	31.623
C(72:28)	3	145	2073.06	0.814	3.626×10^4	14.7326

round trip phase accumulation. The quality factor is given by

$$Q = \frac{\pi n_{neff} L_R}{\lambda} \left(\arcsin \frac{1 - \alpha t + \alpha^2 t^2}{-2\alpha t} \right)^{-1/2} \tag{3}$$

where n_{eff} is the effective refractive index of the fundamental mode, $L_R = 2\pi R + 2L_{MMI}$ is the ring cavity length, λ is the resonance wavelength, and t^2 is field transmission coefficient, which depends on the coupling mechanism between the ring and the bus waveguide.

The ER can be derived from (2):

$$\mathrm{ER} = 10\log\left[\left(\frac{t - \alpha}{1 - \alpha t} \right) \left(\frac{1 + \alpha t}{t + \alpha} \right) \right]^2 \tag{4}$$

where $\alpha^2 = \alpha_c^2 \alpha_R^2$ and α_R^2 is the power transmission coefficient which accounts of solely ring propagation losses. The maximum ER is obtained at the critical coupling condition $\alpha^2 = \alpha_c^2 \alpha_R^2 = t^2$ that corresponds to perfect destructive interference in the bus waveguide due to the resonance in the ring.

Once the optical parameters α_c^2, t^2, and α_R^2 are known by simulations, the expected quality factor Q_{th} and $\mathrm{ER}_{\mathrm{th}}$ can be analytically found by using (3) and (4).

The transmission constant α_R^2 depends on three geometrical parameters: the core width, the curvature radius and the total resonator length L_R. We have derived the coefficient α_R^2 from the scattering matrix of the ring section, which is calculated using the EME method. As mentioned before, the choice of R is strictly related to d_c (and vice versa). In order to have low attenuation constant, both parameters must be chosen in order to ensure as much power as possible in the fundamental mode. From Fig. 5, we have selected $R = 50\ \mu$m in the case of $d_c = 2\ \mu$m($c_T \approx 0.876$) and $R = 145\ \mu$m for $d_c = 3\ \mu$m ($c_T \approx 0.925$). As it can be noticed from Fig. 2(a), the choice of the couplers geometry affects the ring attenuation losses due to changes in total resonator length L_R. Since L_R depends on the MMI configurations, in Table 5 are listed the curvature radii R, the length L_R and the coefficients α_R^2 calculated by considering the three MMI types we analyzed. On the basis of the simulation results and by using the analytical formulas (3) and (4), it is possible to design the resonator and to infer its optical performances by means of a semi-analytical approach. Based on the calculated coefficients, the expected quality factor Q_{th} and extinction ratio ER_{th} are also calculated and reported in Table 5. Hence integrated optofluidic ring resonators with a quality factor of the order of 4×10^4 and high extinction ratio can be obtained, which makes these devices suited for use in sensing applications.

In order to confirm these results we have simulated the spectral response of the ring resonator using a two dimensional finite difference time domain method (2D FDTD) (OMNISIM Photon Design). Since the memory required for the simulation increases very quickly, we limit our attention to ring configuration with bend radius of $R = 50\ \mu$m. The simulated devices are based on
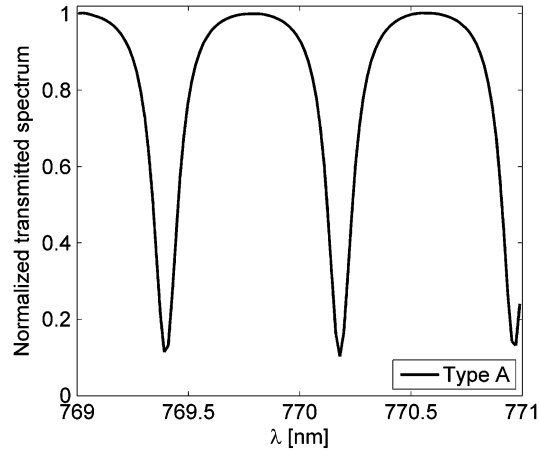
Fig. 6. Simulation result of the normalized transmitted spectrum from type A resonator.
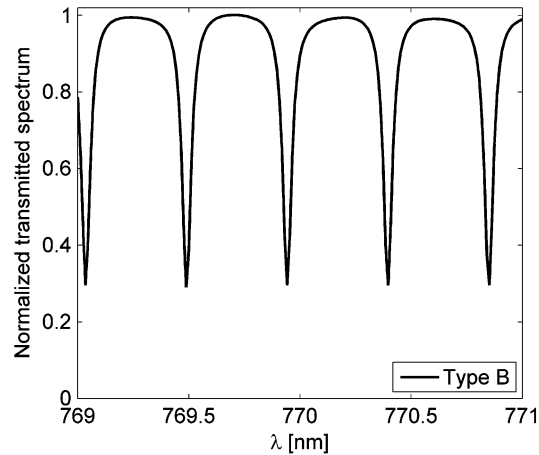

Fig. 7. Simulation result of the normalized transmitted spectrum from type B resonator.

2h-ARROW at working wavelength of $\lambda = 770$ nm with core width $d_c = 2$ μm and refractive index $n_c = 1.330$. Ring devices based on type A, B, and C MMI have been simulated (see Figs. 6–8). The fundamental mode of a 2 μm wide 2h-ARROW waveguide has been assumed as excitation source; it has been modeled as a light pulse centered at $\lambda = 770$ nm with a full width at half maximum (FWHM) linewidth of about 5 nm. Perfectly matched layer (PML) boundary conditions were used at the edge of the computational domain. From the simulated spectra, we have calculated the quality factor Q_{sim}:

$$Q_{\text{sim}} = \frac{\lambda}{\Delta\lambda_{\text{FWHM}}} \tag{5}$$

where $\Delta\lambda_{\text{FWHM}}$ is the full-width at half-maximum of the resonant peaks, and λ is the resonant wavelength, and the extinction ratio ER_{sim}:

$$ER_{\text{sim}} = 10\log\left(\frac{1}{T_{\text{min}}}\right) \tag{6}$$

where T_{min} is the value of the transmitted spectrum calculated at a resonant wavelength. Table 6 lists the calculated parameters. The free spectral range (FSR) is the distance between two consecutive minima (or maxima) in the spectrum.
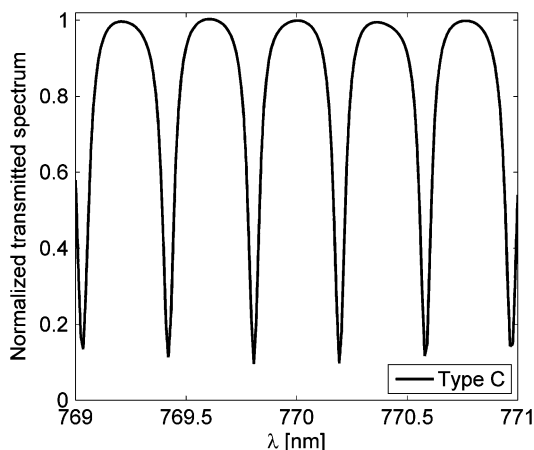
Fig. 8. Simulated normalized transmitted spectrum from ring type C.

TABLE 6

Simulated ring parameters

$Ring\ Type$	Q_{sim}	$ER_{sim}[dB]$	$FSR[nm]$
A(50:50)	6.101×10^3	9.880	0.800
B(85:15)	1.627×10^4	5.398	0.453
C(72:28)	1.360×10^4	11.283	0.386

From Table 6 we can notice that FDTD simulations confirm the expected ring optical behavior. We reach a good agreement between the expected and the simulated values of quality factor.

3. Ring Resonator Sensing Performances

Typically, optical ring resonator sensors are based on refractive index (RI) detection. Mainly, two sensing approaches exploit RI changes: surface sensing and bulk sensing. In both cases the sensing principle is based on effective RI change of the resonant mode which in turns causes a spectral shift of the resonant wavelength. Optical change of the mode effective RI is induced by the presence of the analytes which can be either dispersed in the bulk liquid (bulk sensing) or immobilized on the ring resonator surface (surface sensing). Whatever is the sensing interaction, the sensitivity is strongly affected by the coupling efficiency between the resonant mode and the analytes; maximizing this interaction is one of the main aspect to assess in order to have high sensitivity.

The basic elements of the proposed ring resonator are liquid core hybrid ARROWs. These optofluidic waveguides present the great advantage to have the core channel with double functionality, as it also works as fluidic channel. Thanks to this duality, great compactness and reduced sample consumption can be achieved. The optical mode is well-confined almost in the center of the liquid core. In terms of sensitivity this means that the entire optical mode couples with the liquid sample flowing into the core, resulting in a partial sensitivity $S_p = \partial n_{eff}/\partial n_c = 0.996$. As a counterpart, the mode field intensity at core/cladding interface is very low and only a small fraction of the optical mode interacts with cladding surface. Hence we can expect that the bulk sensitivity is privileged over surface sensitivity.

3.1. Bulk Sensitivity

Theoretical bulk sensitivity can be estimated by evaluating the spectral shift of the resonant wavelength induced by a small variation of the core refractive index n_c. We simulated the
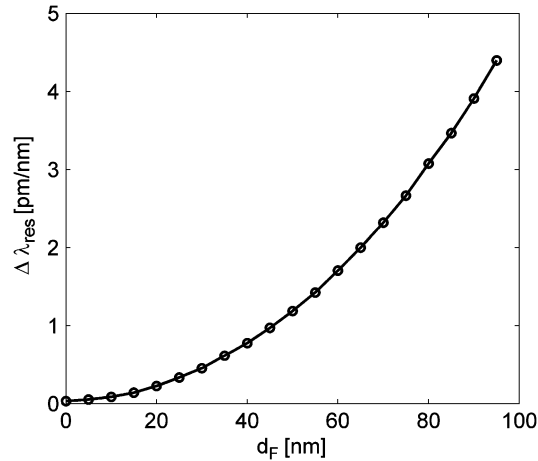
Fig. 9. Surface sensitivity versus adlayer thickness.

spectral response of ring type B by varying the core refractive index; the corresponding resonant spectral shift has been evaluated from the spectrum. We calculated a bulk sensitivity of $S = \Delta\lambda/\Delta n = 640$ nm RIU^{-1}, which rivals with sensitivity demonstrated for other planar integrated ring resonator.

However, the sensing capability of a ring is evaluated on the basis of the minimum detectable refractive index change (Δn_{min}, detection limit) which in turn is related to the smallest detectable wavelength shift $\Delta\lambda_{min}$. Apart from the wavelength resolution of the instrument, accurate experimental detection of wavelength shift mainly depends on the resonant peak full width at half-maximum (FWHM). Sharp resonances are required to increase the accuracy of wavelength shift detection. From the sensitivity definition, the limit of detection is then proportional to FWHM/S. Hence, ring resonators with high Q have better sensitivity, as expected. Based on the simulations and assuming, reasonably, that we are able to detect a spectral change of one twentieth of the resonator linewidth (≈ 2.4 pm), the expected detection limit (LOD)of ring type B with $d_c = 2$ μm is $\Delta n_{min} \approx 3.7 \times 10^{-6}$. The simulated bulk sensitivity and LOD are quite high compared with other optical ring resonators [3], [10], [16], [31], [32]. High LOD in bulk sensing is allowed in a hybrid ARROW thanks to the strong volume interaction between light and fluid core, which is assessed by the partial sensitivity S_p.

3.2. Surface Sensitivity

In order to estimate the surface sensitivity we have evaluated the variation of the effective refractive index of the fundamental mode (n_{eff}) as the thickness of homogeneous layer (d_F) changes. 1-dimensional simulations have been performed by using FDM method. We have assumed a 2h-ARROW with $d_c = 2$ μm and a refractive index for the adlayer of $n_F = 1.45$. Once evaluated n_{eff} versus d_F, the resonance wavelength shift $\Delta\lambda_{res}$ has been derived by using (2).

In Fig. 9 we show the numerical results obtained for the surface sensitivity versus the thickness of adlayer d_F. By taking into account the assumed spectral resolution, reliable surface sensitivity can be obtained only for thick adlayer (upwards to $d_F \approx 60$ nm). Low surface sensitivity in ARROW waveguides is expected due to the weak optical interaction between the fundamental mode and the core walls surface. The propagating mode is well confined in the core volume and only the optical tails reach the core sidewalls, thus limiting the optical coupling. From the analysis of the results we expect the sensing performance can be improved by adding a suitable thin cladding layer on the core sidewalls during the fabrication process. The effect of such an additional layer is to increase the interaction of the field with biolayer [29], [30]. In particular, we have simulated a 2h-ARROW with an extra thin silicon dioxide layer ($n_1 = 1.441$) with thickness of $d_A = 80$ nm. The fundamental mode attenuation loss in this case is $\alpha_0 = 6.82$ cm^{-1}.
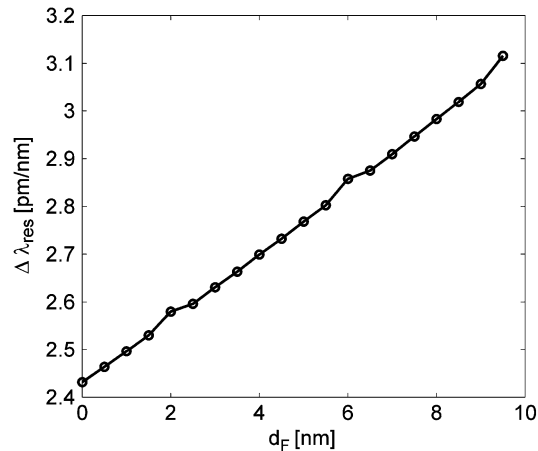
Fig. 10. Surface sensitivity of 2h-ARROW structure with $d_A = 80$ nm versus adlayer thickness.

In Fig. 10 the computed surface sensitivity in a range between 0.1 nm to 10 nm thick adlayer is reported. Surface sensitivity of about $\Delta\lambda_{res} \approx 2.8$ pm/nm is calculated at around $d_F = 5$ nm. With the addition of a suitable thin layer, the surface sensing capability of the proposed device is expected to be comparable with the reported values of other optical ring resonators [3], [10], [31]–[34].

4. Conclusion

In this paper, we report simulation results and design optimization of an integrated planar opto-fluidic ring resonator based on liquid core hybrid ARROWs. Overall the optimization criterion has been the requirement of low propagation losses for a high quality factor ring resonator. The optical properties of hybrid ARROWs have been simulated in order to ensure single mode prop-agation with reduced attenuation losses. A detailed study of the bend ARROW section has been performed which also accounted for the contribution of higher order modes excited in the bend sections. The bending losses have been calculated at different bending radii and core widths. Three different MMI configurations have been studied and considered as coupler ele-ment in the ring layout. The optical performance of ring resonators which differ by MMI coupler has been compared. From simulations we find that quality factor up to 4×10^4 can be obtained. Finally, the sensing performance of the proposed ring has been estimated. In particular, we have calculated a bulk RI detection limit of $\Delta n_{min} \approx 3.7 \times 10^{-6}$.

References

[1] Y. Sun and X. Fan, "Optical ring resonators for biochemical and chemical sensing," *Anal. Bioanal. Chem.*, vol. 399, no. 1, pp. 205–211, Jan. 2011.
[2] C. A. Barrios *et al.*, "Slot-waveguide biochemical sensor," *Opt. Lett.*, vol. 32, no. 21, pp. 3080–3082, Nov. 2007.
[3] C. Y. Chao, W. Fung, and L. J. Guo, "Polymer microring resonators for biochemical sensing applications," *IEEE J. Sel. Topics Quantum Electron.*, vol. 12, no. 1, pp. 134–142, Jan./Feb. 2006.
[4] M. Mancuso, J. M. Goddard, and D. Erickson, "Nanoporous polymer ring resonators for biosensing," *Opt. Exp.*, vol. 20, no. 1, pp. 245–255, Jan. 2012.
[5] N. Jokerst *et al.*, "Chip scale integrated microresonator sensing systems," *J. Biophoton.*, vol. 2, no. 4, pp. 212–226, Apr. 2009.
[6] A. Nitkowski, L. Chen, and M. Lipson, "Cavity-enhanced on-chip absorption spectroscopy using microring resona-tors," *Opt. Exp.*, vol. 16, no. 16, pp. 11930–11036, Aug. 2008.
[7] A. Yariv, "Universal relations for coupling of optical power between microresonators and dielectric waveguides," *Electron. Lett.*, vol. 36, no. 4, pp. 321–322, Feb. 2000.
[8] V. R. Almeida, C. A. Barrios, R. R. Panepucci, and M. Lipson, "All-optical control of light on a silicon chip," *Nature*, vol. 431, no. 7012, pp. 1081–1084, Oct. 2004.
[9] J. Niehusmann *et al.*, "Ultrahigh-quality-factor silicon-on-insulator microring resonator," *Opt. Lett.*, vol. 29, no. 24, pp. 2861–2863, Dec. 2004.

[10] C. F. Carlborg *et al.*, "A packaged optical slot-waveguide ring resonator sensor array for multiplex label-free assays in labs-on-chips," *Lab Chip*, vol. 10, no. 3, pp. 281–290, Feb. 2010.

[11] S. M. Harazim, V. A. Bolaños Quiñones, S. Kiravittaya, S. Sanchez, and O. G. Schmidt, "Lab-in-a-tube: On-chip integration of glass optofluidic ring resonators for label-free sensing applications," *Lab Chip*, vol. 12, no. 15, pp. 2649–2655, Aug. 2012.

[12] E. Ryckeboer *et al.*, "Measurement of small molecule diffusion with an optofluidic silicon chip," *Lab Chip*, vol. 13, no. 22, pp. 4392–4399, Feb. 2013.

[13] D. Psaltis, S. R. Quake, and C. Yang, "Developing optofluidic technology through the fusion of microfluidics and optics," *Nature*, vol. 442, no. 7101, pp. 381–386, Jul. 2006.

[14] X. Fan and I. M. White, "Optofluidic microsystems for chemical and biological analysis," *Nat. Photon.*, vol. 5, no. 10, pp. 591–597, Sep. 2011.

[15] F. Vollmer and S. Arnold, "Whispering-gallery-mode biosensing: Label free detection down to single molecules," *Nat. Methods*, vol. 5, no. 7, pp. 591–596, Jul. 2008.

[16] I. M. White, H. Oveys, and X. Fan, "Liquid-core optical ring-resonator sensors," *Opt. Lett.*, vol. 31, no. 9, pp. 1319–1321, May 2006.

[17] M. Sumetsky, R. S. Windeler, Y. Dulashko, and X. Fan, "Optical liquid ring resonator sensor," *Opt. Exp.*, vol. 15, no. 22, pp. 14376–14381, Oct. 2007.

[18] V. A. B. Quiñones *et al.*, "Localized optical resonances in low refractive index rolled-up microtube cavity for liquid-core optofluidic detection," *Appl. Phys. Lett.*, vol. 101, no. 15, pp. 151107-1–151107-3, Oct. 2012.

[19] G. Testa, Y. Huang, P. M. Sarro, L. Zeni, and R. Bernini, "Integrated silicon optofluidic ring resonator," *Appl. Phys. Lett.*, vol. 97, no. 13, pp. 131110-1–131110-3, Sep. 2010.

[20] G. Testa, Y. Huang, P. M. Sarro, L. Zeni, and R. Bernini, "Liquid core ARROW waveguides by atomic layer deposition," *IEEE Photon. Technol. Lett.*, vol. 22, no. 9, pp. 616–618, May 2010.

[21] D. Yin, J. P. Barber, A. R. Hawkins, and H. Schmidt, "Highly efficient fluorescence detection in picoliter volume," *Appl. Phys. Lett.*, vol. 87, no. 21, pp. 211111-1–211111-3, Nov. 2005.

[22] G. Testa, Y. Huang, L. Zeni, P. M. Sarro, and R. Bernini, "Hybrid silicon-PDMS optofluidic ARROW waveguide," *IEEE Photon. Technol. Lett.*, vol. 24, no. 15, pp. 1307–1309, Aug. 2012.

[23] G. Testa, G. Persichetti, P. M. Sarro, and R. Bernini, "A hybrid silicon-PDMS optofluidic platform for sensing applications," *Biomed. Opt. Exp.*, vol. 5, no. 2, pp. 417–426, Jan. 2014.

[24] H. Schmidt, D. Yin, J. P. Barber, and A. R. Hawkins, "Hollow-core waveguides and 2-D waveguide arrays for integrated optics of gases and liquids," *IEEE J. Sel. Topics Quantum Electron.*, vol. 11, no. 2, pp. 519–526, Mar./Apr. 2005.

[25] G. Testa, Y. Huang, L. Zeni, P. M. Sarro, and R. Bernini, "High visibility integrated optofluidic Mach-Zehnder interferometer," *Opt. Lett.*, vol. 35, no. 10, pp. 1584–1586, May 2010.

[26] N. M. Litchinitser, A. K. Abeeluck, C. Headley, and B. J. Eggleton, "Antiresonant reflecting photonic crystal optical waveguides," *Opt. Lett.*, vol. 27, no. 18, pp. 1592–1594, Sep. 2002.

[27] J. L. Archambault, R. J. Balck, S. Lacroix, and J. Bures, "Loss calculations for antiresonant waveguides," *J. Lightw. Technol.*, vol. 11, no. 3, pp. 416–423, Mar. 1993.

[28] L. B. Soldano and E. C. M. Pennings, "Optical multimode interference devices based on self-imaging: Principles and applications," *J. Lightw. Technol.*, vol. 13, no. 4, pp. 615–627, Apr. 1994.

[29] J. Canning *et al.*, "Manipulating and controlling the evanescent field within optical waveguides using high index nanolayers," *Opt. Mater. Exp.*, vol. 1, no. 2, pp. 192–200, Jun. 2011.

[30] G. R. Quigley, R. D. Harris, and J. S. Wilkinson, "Sensitivity enhancement of integrated optical sensors by use of thin high-index films," *Appl. Opt.*, vol. 38, no. 28, pp. 6036–6039, Oct. 1999.

[31] X. Fan, I. M. White, H. Zhu, J. D. Suter, and H. Oveys, "Overview of novel integrated optical ring resonator bio/chemical sensors," *Proc. SPIE*, vol. 6452, pp. 64520M-1–64520M-20, 2007.

[32] H. Li and X. Fan, "Characterization of sensing capability of optofluidic ring resonator biosensors," *Appl. Phys. Lett.*, vol. 97, no. 1, pp. 011105-1–011105-3, Jul. 2010.

[33] H. Zhu, I. M. White, J. D. Suter, P. S. Dale, and X. Fan, "Analysis of biomolecule detection with optofluidic ring resonator sensors," *Opt. Exp.*, vol. 15, no. 15, pp. 9139–9146, Jul. 2007.

[34] J. T. Gohringa, P. S. Daleb, and X. Fan, "Detection of HER2 breast cancer biomarker using the opto-fluidic ring resonator biosensor," *Sens. Actuators B, Chem.*, vol. 146, no. 1, pp. 226–230, Apr. 2010.